Journal of Cleaner Production 372 (2022) 133755

Contents lists available at ScienceDirect

Journal of Cleaner Production

journal homepage: www.elsevier.com/locate/jclepro

Hydrogen plasma smelting reduction process monitoring with optical emission spectroscopy – Establishing the basis for the method

Henri Pauna [a,*], Daniel Ernst [b], Michael Zarl [c], Matti Aula [a], Johannes Schenk [b,c], Marko Huttula [d], Timo Fabritius [a]

[a] Process Metallurgy Research Unit, P.O. Box 4300, FI-90014, University of Oulu, Finland
[b] Department of Metallurgy, Chair of Ferrous Metallurgy, Montanuniversitaet Leoben, 8700, Leoben, Austria
[c] K1-MET GmbH, Stahlstraße 14, A-4020 Linz, Austria
[d] Nano and Molecular Systems Research Unit, P.O. Box 3000, FI-90014, University of Oulu, Finland

ARTICLE INFO

Handling Editor: Panos Seferlis

Keywords:
Hydrogen plasma smelting reduction
Optical emission spectroscopy
Plasma analytics
Process control

ABSTRACT

In the world of ever-increasing demand for carbon-free steel, hydrogen and recycling have an undeniable role in achieving net-zero carbon dioxide emissions for the steel industry. However, even though steel is one of the most recycled materials globally, the quantity of steel that can be made from recycled steel will probably not match the demand in the future. This in turn means that steel must be also produced from the conventional resource, the iron ore. Hydrogen has been proposed as an environmentally friendly alternative to carbon as a reducing agent. To tackle the problems related to the usage of hydrogen for this purpose, hydrogen plasma smelting reduction has been studied extensively in the last few years. This article aims to provide means for process control of the hydrogen plasma, which may show erratic and chaotic behavior during the smelting process. The method used is optical emission spectroscopy, with which the plasma can be characterized, its composition can be evaluated, and its temporal evolution can be assessed. This study sheds light on how the plasma behaves with different electrode gaps and flow gas compositions together with how the position of the arc with respect to the center of the crucible can be assessed. In Ar/H_2 plasma, the plasma temperatures derived with OES varied between 4000 and 10000 K, and up to a 26% decrease in electron density was observed when increasing the electrode gap in 1 cm increments.

1. Introduction

Climate change and its enormous impact on the environment prompted the European Union with the European Green Deal (EGD) to become the first carbon-neutral continent by 2050 and reduce greenhouse gas (GHG) emissions by at least 55% by 2030 compared to 1990 (Hainsch et al., 2022; Chauvy and Weireld, 2020; Rieger et al., 2021). This ambitious target also urges the European steel industry to optimize or replace its dominant process routes. Worldwide 4–5% of the total GHG and about 7% of all anthropogenic CO_2 emissions are caused by the iron and steel industry (Zhao et al., 2020; Quader et al., 2015; Draxler et al., 2020; Holappa, 2020). The so-called integrated route produces the largest proportion (70%) of the steel via the blast furnace (BF) and basic oxygen furnace (BOF), followed by the recycling route using electric arc furnaces (EAF) with approximately 25%. The remaining 5% is produced via direct or smelting reduction (Draxler et al., 2020; Suopajärvi et al., 2018). 2020 worldwide more than 1.87 billion tons of steel were mainly produced via these routes with an annual growth of 3% between 2015 and 2020 (World Steel Association AISBL, 2021). The integrated route (BF–BOF) emits approximately 1.8 t CO_2 per ton of crude steel, which is not particularly high compared to the production of other metals but leads to a large contribution to GHG emissions due to the huge production volumes involved. 90% of these emissions are caused only by the sintering, coking, and blast furnace processes, whereby the BF has an energy demand and is accompanied by CO_2 emissions of 12.31 GJ/tHM and 1.22 tCO_2/tHM (Quader et al., 2015; Suopajärvi et al., 2018). To fulfill the aims of the European Green Deal, the iron and steel industry is forced to create strategies to reduce GHG emissions. For this target, two main technological pathways are pursued. Smart Carbon Usage (SCU) includes Process Integration (PI) and Carbon Capture and Utilization (CCU). PI aims to modify the existing iron and steelmaking routes to reduce carbon input and CO_2 emissions. CCU focuses on CO_2 capture

* Corresponding author.
E-mail address: henri.pauna@oulu.fi (H. Pauna).

https://doi.org/10.1016/j.jclepro.2022.133755
Received 26 April 2022; Received in revised form 7 August 2022; Accepted 19 August 2022
Available online 24 August 2022

from the waste gases to produce basic chemicals, e.g., catalytic conversion processes. The second pathway is Carbon Direct Avoidance (CDA) which aims to develop new steel production routes without directly releasing carbon emissions. For this purpose, these technologies use renewable electricity or green hydrogen or both (Draxler et al., 2020; Eurofer The European Steel Association, 2019).

Hydrogen Plasma Smelting Reduction (HPSR) is one of these key technologies to achieve the necessary GHG reduction. In this process, a plasma arc is ignited between a hollow graphite electrode (cathode) and the melted pool (anode). Iron ore fines, hydrogen, and argon are introduced via the electrode into the reduction zone during this procedure. The charged ore is melted inflight and reduced to metallic iron with excited and ionized hydrogen species producing steam as a by-product (Zarl et al., 2020; NaseriSeftejani and Schenk, 2018a, 2018b). A recent comprehensive study by Souza Filho et al. (Souza Filho et al., 2022) considers the usage of hydrogen from a wider perspective, where the initial reduction would be done with direct reduction and the rest with HPSR in order to increase the efficiency of the reduction and minimize the H_2 usage.

A transferred plasma arc is present in the HPSR process. Collisions, radiation-activated processes, and recombination trigger several intermediates such as atomic or excited hydrogen. When the molecular H_2 is supplied with sufficient energy, it transforms into excited hydrogen molecules (H_2*), atomic hydrogen (H), and ionic hydrogen (H^+) (Sabat and Murphy, 2017). In addition, there are further hydrogen forms during the transition to the ionized species, $H^+ > H_2^+ > H_3^+ > H > H_2$, whose reduction potential decreases from left to right (Zarl et al., 2020). Due to this fact, the composition and properties of the hydrogen plasma are of significant interest.

In this study, plasma within an HPSR furnace is studied with optical emission spectroscopy (OES) using both pure argon gas and Ar/H_2 gas mixture. The plasma temperature and the electron densities are calculated using the OES data. Individual elements and the time evolution of the optical emissions are identified from the spectra and used to analyze the behavior of the arc. Finally, the arc's stability and movements are concluded with the plasma reactor's electrical data, OES data, and camera images. It is found that the arc's position in the furnace can be evaluated from the OES spectra. The temporal evolution of the spectra and plasma parameters, on the other hand, gives insight into the behavior of the gas, steel, and impurity components in the process. To the best of the authors' knowledge, this is the first study aimed toward a more profound understanding of the HPSR and optimizing the process by the means of OES.

2. Methods and materials

The plasma furnace, located at the Chair of Ferrous Metallurgy at the Montanuniversitaet of Leoben, consists of a power supply unit, a flow control system for the plasma gas supply, the furnace vessel, a mass spectrometer for exhaust gas analysis, and an optical spectrometer (Zarl et al., 2020; NaseriSeftejani and Schenk, 2018a, 2018b). The DC power supply unit was manufactured from Messer Grießheim GmbH. These consist of a transformer with a downstream rectifier. The maximum output power at a voltage of 100 V and a current of 160 A is 16 kVA. The power can be adjusted in two stages (power levels 1 and 2). The plasma gas composition is controlled by two "EL-FLOW PRESTIGE F–201C" mass flow controllers from Bronkhorst High-Tech BV. These can provide hydrogen and argon in quantities of up to 10 l/min each, where a total flow rate of 5 l/min is not exceeded in the trials. The quality of the used gases can be obtained from Table 1.

Table 1
Qualities of the gases used for the trials (Zarl et al., 2020).

Gas	Purity	Remarks
H_2	5.0	–
Ar	5.0	O_2, N_2, $H_2O \leq 5$ ppm

The furnace vessel consists of a bottom part and a removable lid. The water-cooled and refractory-lined lid has five openings, each with a flange connection welded to it. The first flange serves as an observation opening with a sight glass. The "Axis-Q1775" camera from Axis Communications AB records the furnace chamber and transmits the images to a connected computer in real-time. On another flange is a pressure gauge for checking the total pressure in the furnace vessel. The third opening was provided for future expansion and is meanwhile closed with a cylindrical cover plate. The exhaust gas again escapes through a cover opening and enters an attached heated hot gas filter, type "FE2" from ABB Ltd. The cathode is introduced into the furnace chamber through the central cover flange. The graphite cathode with an outer diameter of 26 mm, is located in a double-jacketed water-cooled guiding cylinder, allowing vertical electrode movement using a spindle shaft motor next to the reactor vessel. The graphite cathode has a Ø5 mm central hole along the cylinder axis through which the plasma gas and continuously charged ore enter the furnace chamber. A 10 × 20 mm step was fabricated at the end of the electrode to improve arc stability. In the water-cooled and refractory-lined lower vessel of the furnace are the steel bottom anode and on top of it the steel crucible. The crucible consists of a cylindrical bottom and an attached hollow cylinder as a vessel wall. The exact dimensions are given in Fig. 1 and the chemical analysis in Table 2.

The quadrupole mass spectrometer GAM 200 from the company InProcess Instruments Gesellschaft für Prozessanalytik GmbH is used for exhaust gas analysis. After the hot exhaust filter, a portion of the exhaust gas flows into the mass spectrometer, where various components are heated to prevent the condensation of water vapor.

On the side of the lower part of the furnace is an opening for the OES measurement. The spectrometer tunnel consists of sight glass, a series of flanges and gaskets, and an adjustable holder for the fiber optic cable. The mount fixes the fiber optic cable in position and has been aligned so that the entrance of the fiber optic cable points as directly as possible into the plasma beam. A sketch of the setup for spectrum measurement is shown in Fig. 2.

The spectrometer used, from the company Avantes BV, has three channels. It consists of three individual "AvaSpec-ULS3648-USB2-RM" spectrometers, which measure different wavelength ranges combined in one housing. The first spectrometer records in the wavelength range from 300 nm to 535 nm. It has a "UC" diffraction grating with 1200 lines/mm and a filter ("OSF-305″) to cancel higher-order diffracted lines before the detector. The second spectrometer covers the wavelength range from 530 nm to 742 nm and is equipped with a "VC" diffraction grating (1200 lines/mm) and an "OSF-515″ filter. Spectrometer No. 3 measures in the wavelength range from 740 nm to 1040 nm, and has an "SI" diffraction grating with 830 lines/mm and an "OSF-600″ filter. All three spectrometers have a "DCL-UV/VIS-200″ detector lens to increase sensitivity and a "Toshiba TCD 1304″ detector with 16-bit analog-to-digital converter. The beam entrance slit has a diameter of 10 μm and a focal length of 75 mm. The resolution of the first and second spectrometer is 0.18 nm and 0.25 nm for the third. The fiber optic cable

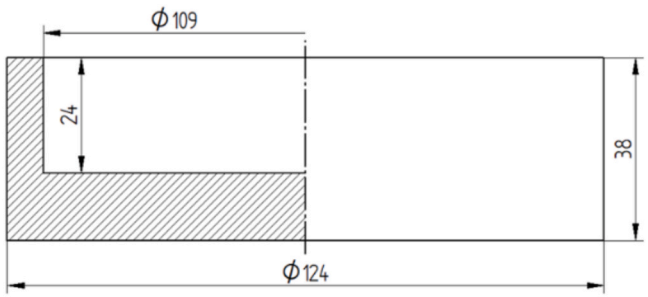

Fig. 1. Quarter section of the crucible dimensions [mm].

Table 2
Chemical composition of the steel crucible.

Element	wt(%)
Fe	97.6
Mn	1.41
Si	0.224
Cu	0.215
Cr	0.187
C	0.129
Ca	0.0033

connected to each spectrometer channel is 2 m long. At half the length, the three individual cables (each 600 μm in diameter) are joined into one, at the end of which a 6 mm diameter converging lens is mounted. This end is attached to the furnace as described above.

In this study, eight experiments, labeled as E1-E8, were conducted with varying parameters. Table 3 lists the electrode gaps, Ar and H_2 content, power level (PL), and duration of the experiments E1-E8. Two PLs with 100 and 160 A currents will be referred to as PL1 and PL2, respectively. For a detailed description of the HPSR together with an evaluation of which parameters affect the overall reduction process and a comparison of HPSR with results in the literature, the readers are directed to the earlier works of Ernst (Zarl et al., 2022) and Zarl (Ernst et al., 2022).

3. Theoretical

The high energy of the plasma decomposes material into both neutral and ionized atoms and molecules. Some of this energy is transferred to these particles, where their electrons get excited to higher energy states. The excited state of a particle is not stable, and thus the particle relaxes back towards its lowest energy state. In addition to collisional and non-radiative relaxation processes, the particle may release the energy as a photon. The photon's energy, which is inversely proportional to the wavelength, equals the energy difference between the upper and lower energy states.

Due to the unique structure of each element and molecule, the photon energies are characteristic of each particle. Because of this, multiple species that radiate simultaneously in the plasma can be identified from an optical emission spectrum where the intensities of the optical emissions are presented with respect to wavelength. Atomic optical emission lines are labeled with the element symbol followed by a Roman numeral describing the ionization degree of the atom. A neutral atom is labeled with I, a singly ionized atom with II, and so on.

Two of the most common parameters that are used to characterize and analyze plasma are temperature and electron density. Plasma temperature affects the optical spectra because higher plasma temperature excites the particles to higher energy states and vice versa, and thus emission line intensities will change with changing plasma temperature. The plasma temperature can be calculated with Boltzmann equation by measuring the wavelength-integrated line intensities (Aragón and Aguilera, 2008). This equation reads

$$ln\left(\frac{\varepsilon^z \lambda_{mn}}{g_m A_{mn}}\right) = -\frac{1}{kT}E_m^z + ln\left(\frac{hcN^z}{4\pi U^z(T)}\right) \quad (1)$$

where z is the ionization state of the radiating species, ε^z is the wavelength-integrated emissivity that is proportional to the line intensity when the plasma is in local thermodynamic equilibrium (LTE), lambda is the wavelength of the emission line, subscripts n and m denote the lower and upper energy levels of the atom, respectively, g is the degeneracy of the energy level, A_{mn} is the transition probability, k is the Boltzmann constant, T is the temperature, and E is the energy of an energy level. The Boltzmann plot is formed by first measuring multiple emission line intensities ε^z from the OES spectra and then calculating the left-hand-side of the Equation (1) for each optical emission line. When E_m^z is plotted as the function of the left-hand-side of Equation (1), the temperature can be calculated from the slope of the linear fit to the datapoints. The logarithmic term with Planck's constant h, speed of light c, number density N, and partition function $U^z(T)$, is a constant at a given temperature and thus can be neglected. The Ar I and H I lines used in the plasma temperature analysis are in Table 4.

Electron density describes the number of electrons per volume of the plasma. In this work, the electron density has been evaluated with the full width at half maximum (FWHM) of the H_α line. The higher the electron density is, the wider the FWHM becomes due to collisions between the electrons and particles within the plasma. The electron density has been estimated with the FWHM value of H_α by using the empirical equation from the work of D. M. Surmick and C. G. Parigger

Table 3
Experiment details for E1-E8.

E#	Electrode gap [mm]	Target Ar-%	Target H_2-%	Power Level	Time [s]
1	30	100	0	1	300
2	40	100	0	1	300
3	50	100	0	1	300
4	60	100	0	1	300
5	30	60	40	1	264
6	40	60	40	1	222
7	40	60	40	2	300
8	50	60	40	2	333

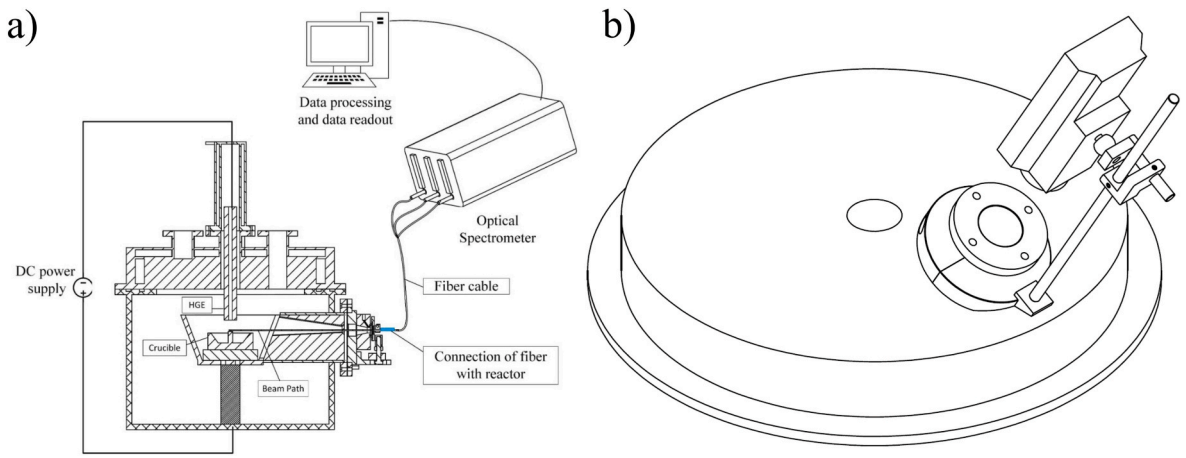

Fig. 2. a) Laboratory reactor with OES analysis (Masab Naseri Seftejani, 2020), and b) camera position outside the furnace (Zarl et al., 2020). HGE stands for hollow graphite electrode.

Table 4
Optical emission lines used for plasma temperature analysis.

Line	λ_{mn} (nm)	A_{mn} (s^{-1})	E_m^z (eV)	g_m	Notation
Ar I	415.859	1.40E+06	14.53	5	–
Ar I	420.067	9.70E+05	14.50	7	–
Ar I	696.543	6.40E+06	13.33	3	–
Ar I	706.722	3.80E+06	13.30	5	–
Ar I	714.704	6.30E+05	13.28	3	–
Ar I	727.294	1.83E+06	13.33	3	–
H I	434.047	2.53E+06	13.05	50	γ
H I	486.135	8.42E+06	12.75	32	β
H I	656.279	4.41E+07	12.09	18	α

(Surmick and Parigger, 2014), where they studied the line widths of H_α and H_β lines for laser-induced plasma. The equation reads

$$N_e = 10^{17} \times \left(\frac{H_{\alpha,FWHM}[nm]}{1.3}\right)^{1/C} \quad (2)$$

where C is constant depicting either the upper or lower limit with values of 0.61 and 0.67, respectively. The lower limit with 0.61 was used in this study. The results of Equation (2) are used as rough estimates of the electron density. The emphasis is on assessing how the electron density changes with different electrode gaps and gas compositions rather than deriving exact values.

When the LTE conditions do not hold for the plasma and the atmosphere is optically thick, i.e. absorbs light effectively, the spectrum will be distorted to some extent due to the absorption of light by the atmosphere. Absorption can also happen if e.g. an Ar atom near the core of the plasma emits a photon that is absorbed by another Ar atom near the edges of the plasma, a phenomenon called self-absorption (SA). SA is quite common in plasmas where the content of a constituent within the plasma is high, for example, Ar and H_2 in this case. Generally, SA affects the most intensive emission lines, whereas low-intensity emission lines remain mostly unaffected. Thus, a low-intensity emission line that is not prone to SA was selected as a reference line for an SA compensation algorithm to study the effect of SA on plasma temperatures.

First, the plasma temperature T_{plasma} was calculated with Equation (1) and that temperature was used as a starting point for the algorithm. Then, the intensity of the reference line was used to calculate the theoretical intensity of the other emission lines using the T_{plasma}. A new plasma temperature was calculated using these new line intensities. If coefficient of determination $R^2 > 0.95$ was achieved for the Boltzmann plot, the T_{plasma} was taken as a corrected plasma temperature. If R^2 was lower than 0.95 after 100 iterations, it was assumed that SA made the temperature analysis unreliable for that instance. These instances were disregarded in the temperature analysis. However, when the SA algorithm converged, it provided temperatures that were on average 500 K lower than the original temperatures. This is an expected result since the SA decreases the intensity of those lines with the lowest excitation energies (Sun and Yu, 2009), which in turn results in lower plasma temperatures when calculated with Equation (1). An example of Lorentzian fit to H_α line, Boltzmann plot, and flowchart for the algorithm is displayed in Fig. 3. The temperatures that have been presented in this article are those that were analyzed with the SA algorithm.

4. Results and discussion

Fig. 4 depicts example spectra and arc images from several experiments with both 40 mm and 50 mm electrode gaps. All spectrum intensities have been normalized to the same intensity value for better comparison because the high intensity of the Ar and H_α lines would otherwise make fainter lines unnoticeable. As can be seen from the arc images, the arc emits mainly bright white light when there is only argon in the gas mixture, whereas the arc's color shifts to red when hydrogen is added to the mixture. Argon has a magnitude of emission lines from UV to near-infrared, and thus the integrated color emitted by argon appears white. On the other hand, hydrogen has only four intensive emission lines, the most intensive one being H_α followed by H_β at 656 and 483 nm, respectively. The line at 656 nm makes the argon/H_2 mixture glow red especially at the edges of the arc, whereas the center where the temperature is higher emits white light due to argon.

The instances in Fig. 4 have been selected to showcase different electrode gaps, gas mixtures, and spectral characteristics. For example, a) - d) with pure argon show very similar spectra with one another, where b) and d) have high Fe I emissions in the spectra which can be seen as a blue glow in the arc images. e), f), and h) show near-center arcs for Ar/H_2 mixture. g), i), and j) showcase CaO optical emissions, clear melt at the bottom of the crucible, and high Fe I emissions, respectively. The molecular optical emissions from the CaO may originate from residues of iron ore in the graphite electrode which were then introduced by the gas flow into the crucible. The time evolution of various steel and slag species will be addressed later in this article.

Fig. 4 also shows a drastic change in the Ar I emission lines when H_2 is added to the gas flow. Fig. 4 a) - d) have very intensive Ar I lines between 670 and 900 nm, whereas their intensity drops significantly in e) - j) with the addition of H_2. A similar decrease of Ar I lines with the addition of H_2 has been reported by Mauer (2021) for low-pressure plasma, where they concluded that the addition of even a few percent hydrogen promotes recombination processes and that the loss of Ar I lines is partly attributed to recombination process. In these reactions, $Ar^+ + H_2 \rightarrow ArH^+ + H$ followed by $ArH^+ + e^- \rightarrow Ar + H^*$ have a key role (* denotes an excited state).

Fig. 5 a) and b) display the relation between the voltage and the arc length when the arc is directly at the center of the crucible, i.e. when the

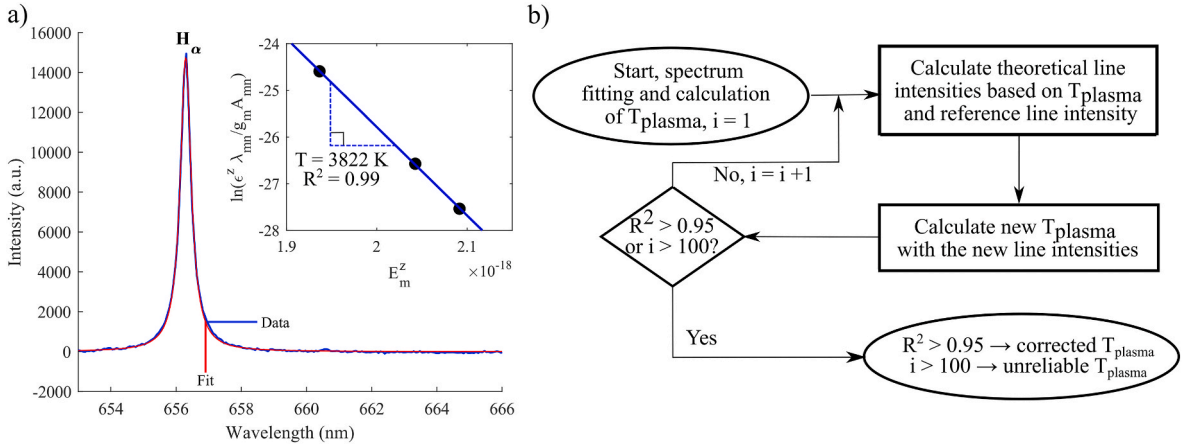

Fig. 3. a) Lorentz fit to H_α line and Boltzmann plot for calculation of plasma temperature with Equation (1), and b) flowchart of the SA algorithm.

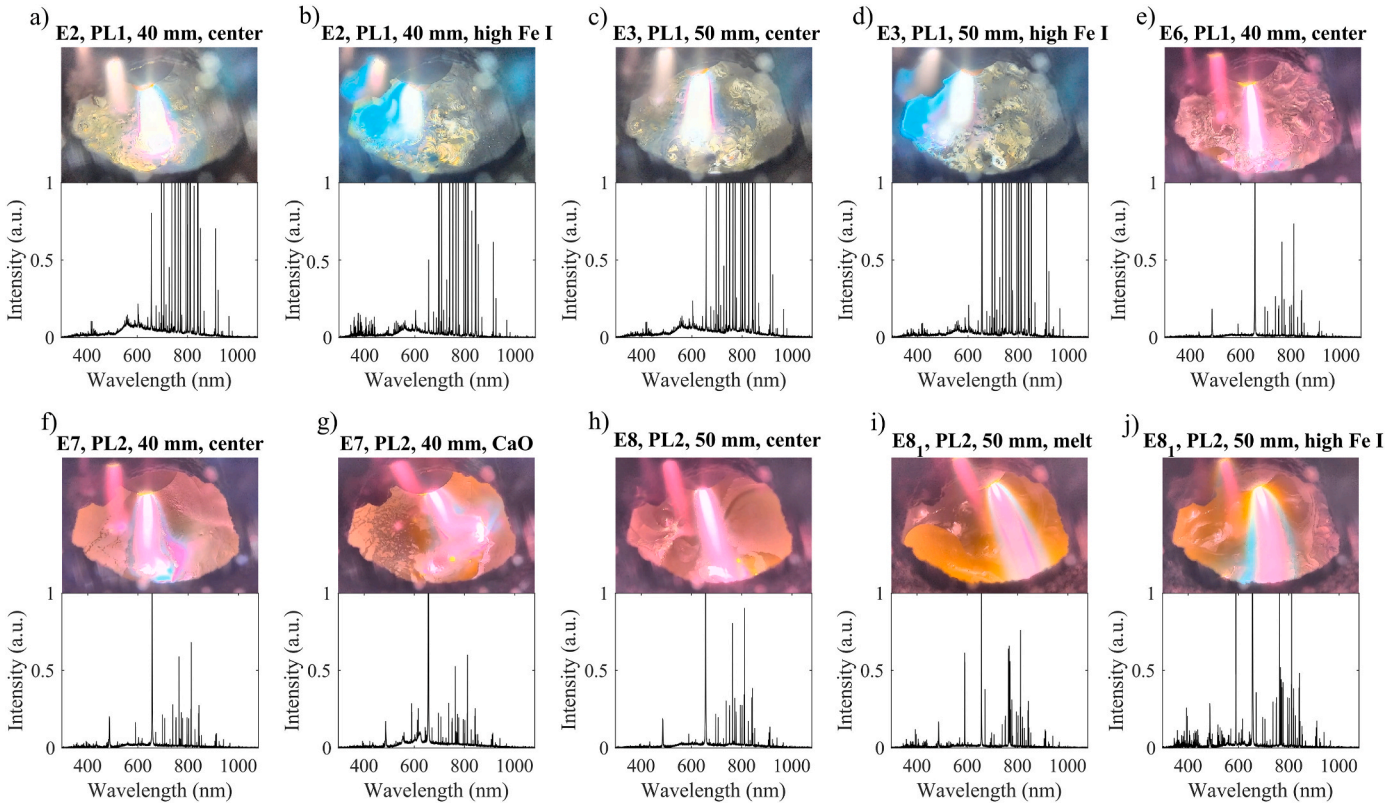

Fig. 4. Example spectra and arc images from various instances with a) – d) 100% Ar (PL1), e) 60% Ar and 40% H_2 (PL1), and f) – j) 60% Ar and 40% H_2 (PL2). The spectrum intensities have been capped at 10 000 a.u. and normalized for better readability of the weaker emission lines and easier comparison. The arc extinguished during E8, and the arc images and spectra after the arc was reignited are marked with E8$_1$.

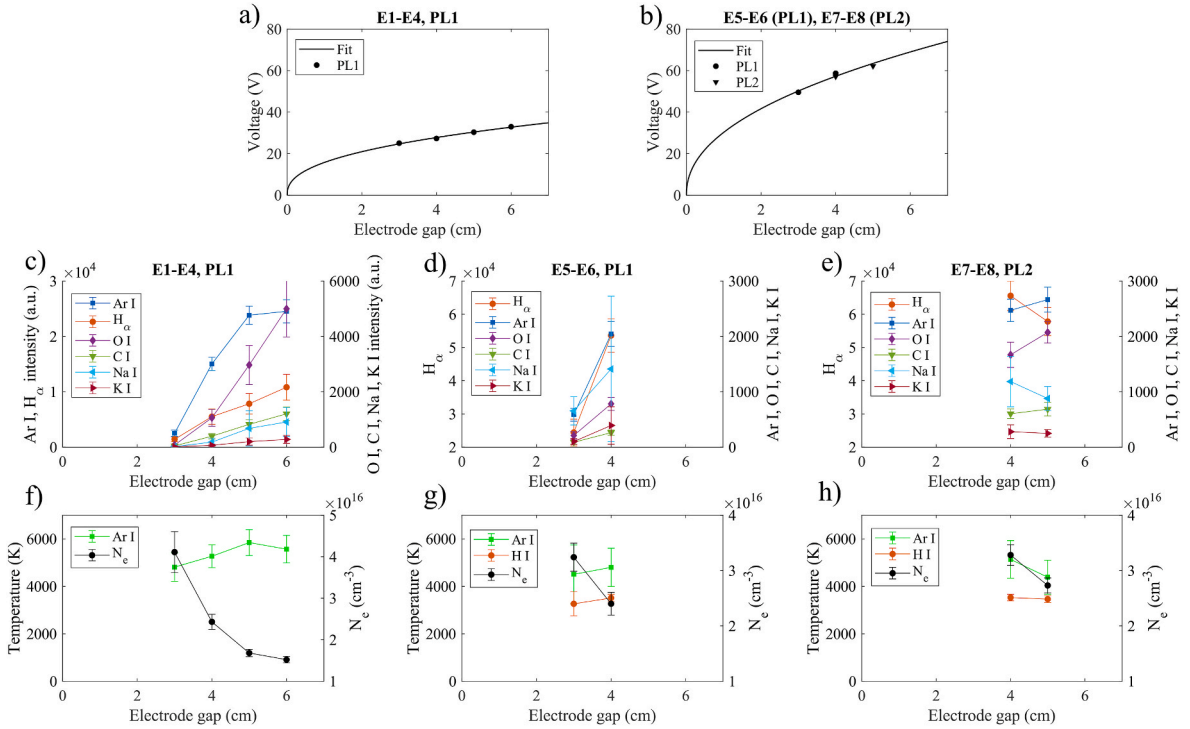

Fig. 5. Minimum voltage when the arc is in the center of the crucible as a function of electrode gap for a) E1-E4 and b) E5-E8 together with mean emission line intensities for c) E1-E4, d) E5-E6, and e) E7-E8, and electron density, Ar and H plasma temperatures for f) E1-E4, g) E5-E6, and h) E7-E8. The error bars in c) – h) indicate the standard deviation for each species.

arc length equals the electrode gap, for E1-E4 and E5-E8, respectively. The best fit to the data was deduced to be a simple power function of the form $Voltage = A \times l_{arc}^{B}$, where A and B are constants. Fig. 5 c) – h) show the mean values for various emission lines, plasma temperature, and electron density deduced from the spectra for E1-E4 (PL1), E5-E6 (PL1), and E7-E8 (PL2). The error bars in the c) – h) illustrate the standard deviation throughout the experiment in question. The emission lines in the c) are quite uniform since all the emission line intensities increase with the increasing electrode gap. Ar plasma temperature increases until a drop towards 6 cm gap, and the electron density decreases with increasing electrode gap. Decreasing electron density, and thus also decreasing FWHM of the H emission line, is expected since the arc's volume also increases as its length increases. The trends of Ar/H_2 mixtures of Fig. 5 d) are like those in c), but some intensities drop in e) with a higher power level. Furthermore, the electron density increases with the same electrode gap when the power level is higher.

The plasma temperatures derived with Ar and H emission lines do not show clear trends in Fig. 5 f) – h) with respect to the changing electrode gap. One of the reasons for this is that the arc wanders around the crucible, resulting in the erratic temporal evolution of the plasma parameters. Additionally, the higher the electrode gap, the more the arc moves to the outer areas of the crucible. The temporal variations of the plasma temperatures due to arc movement, and thus also varying length of the arc, have a significant effect on the mean values. However, the electron densities and FWHM of the H emission line decrease with increasing electrode gap.

Even though the gas flow consisted of pure Ar in E1-E4, H I emission lines are clearly seen in the spectra. Fig. 6 shows the relationship between H_α, O I, and C I between different experiments. There is a clear increasing trend for all these components with respect to each other in E1-E6, whereas this relation holds only between O I and C I for E7 and E8. When there is no H_2 in the gas flow, the source of hydrogen optical emissions is most probably the residual water vapor in the atmosphere. Similar trends between H, C, and O optical emissions could mean a common origin, i.e. the residuals and air in the furnace. As can be seen from Fig. 6 d) – i), the correlation between H and O together with O and C deteriorates as H_2 is added to the mix and the power level is increased, whereas O I and C I correlation prevails.

As an example of the time evolution of various parameters during an experiment, Fig. 7 shows the time evolution of several emission lines, plasma diagnostics, and electrical data of the furnace together with exhaust gas content for Ar and H_2. As can be seen from the figure, Ar I emissions stay at a relatively constant value, whereas hydrogen lines gradually decrease as the experiment proceeds. On the other hand, O I increases towards the end of the experiment, and Na I and K I emissions peak frequently during the experiment. C I intensities stay at a near-constant values. Ar I plasma temperature fluctuates between 4000 and 8000 K, with several gaps indicating poor plasma diagnostics conditions. The gaps arise because the self-absorption algorithm does not converge, suggesting that these instances have higher self-absorption of argon lines. H I plasma temperature, on the other hand, is between 3000 and 4000 K, with a slightly declining trend towards the end of the experiment.

To compare the time evolution of optical emission lines in different experiments, Fig. 8 showcases the temporal evolution and intensity of H I, Ar I, O I, C I, and Na I by comparing a) E2 and E7, and b) E3 and E8. E2

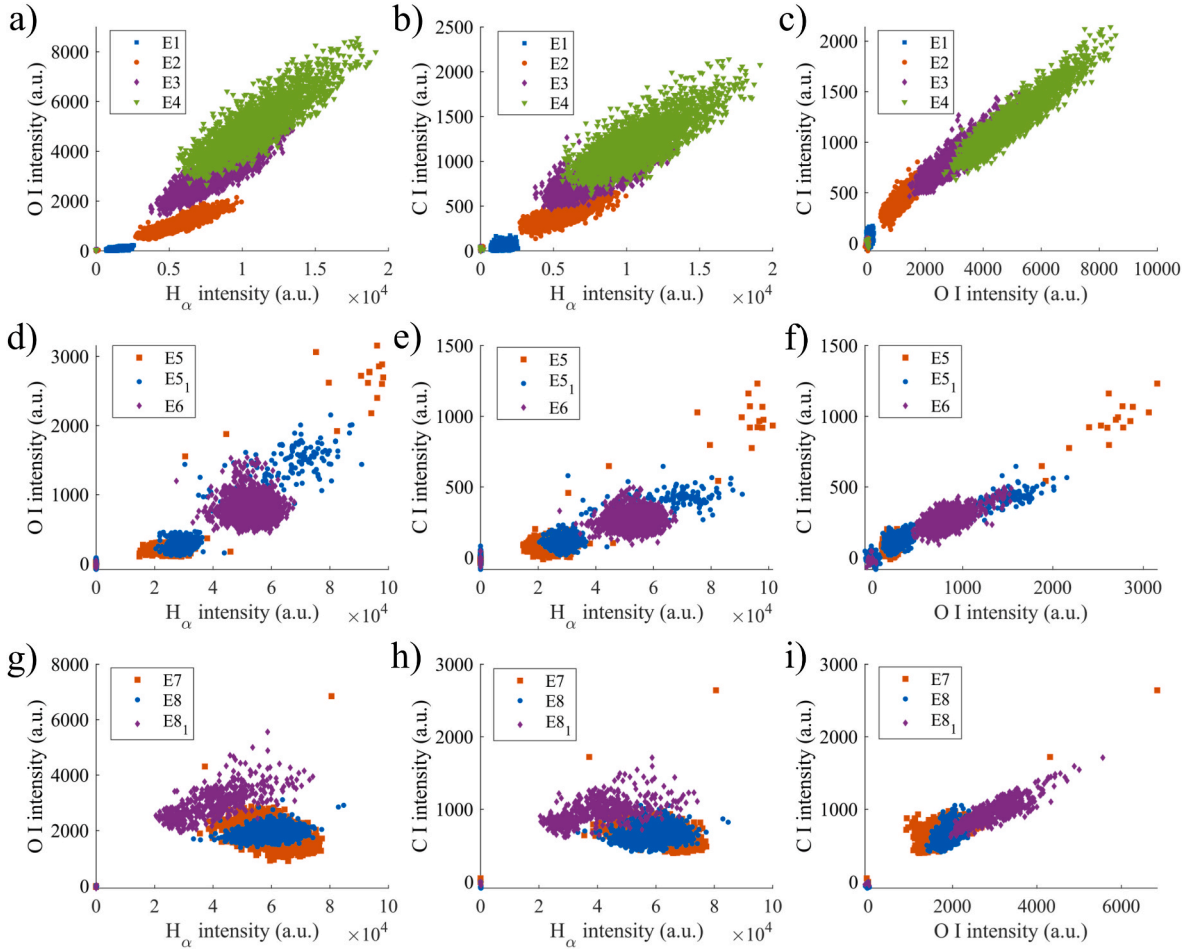

Fig. 6. Relations between H_α, O I, and C I for a) - c) E1-E4, d) - f) E5-E6, and g) - i) E7-E8. The E5 and E8 have been split to two instances differentiated by subscript. Arc extinguished during these experiments, and $E5_1$ and $E8_1$ are the datapoints after the arc was reignited.

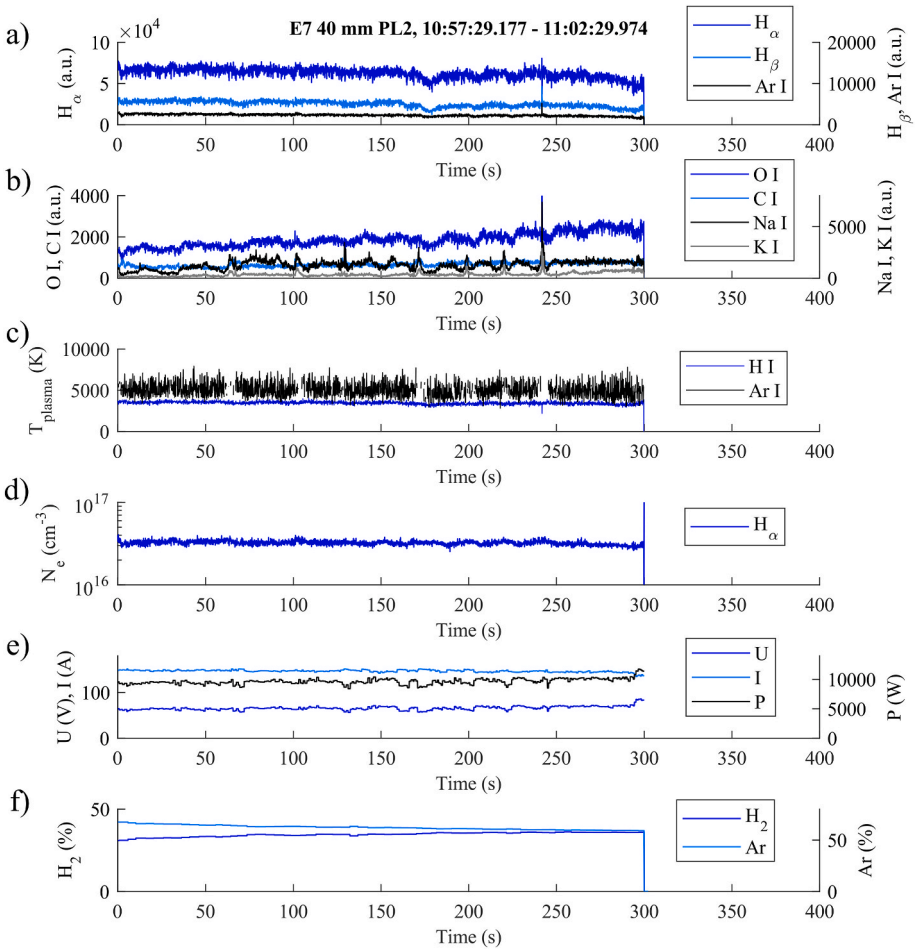

Fig. 7. E7's time evolution for a) H_α, H_β, and Ar I intensities, b) O I, C I, Na I, and K I intensities, c) H I and Ar I plasma temperatures, d) estimate of N_e using H_α FWHM, e) voltage, current, and power, and f) H_2 and Ar content in the exhaust-gas.

and E7 have the same electrode gap of 40 mm, whereas the electrode gap is 50 mm for the E3 and E8. E2 and E3 have pure argon in the gas mixture, and E7 and E8 have nearly 40% hydrogen in the mixture. Generally, the Ar lines dominate the spectra with 100% argon, but H_α line intensity tops everything in the spectra when H_2 content is 40%. O I and C I are quite similar between different gas mixtures, but the average Na I emission line intensities increase significantly once H_2 is present in the gas.

Even though the crucible of the furnace is made of steel, remnants of common slag components, such as calcium, magnesium, and manganese were present in the spectra in addition to iron and chromium. Like Figs. 8 and 9 shows the time evolution of Fe I, Ca II, Mg I, Cr I, and Mn I emission line intensities for a) E2 and E7, and b) E3 and E8. A closer look at the iron emission line intensities reveals that the optical emissions from iron atoms are present in most of the spectra when there is only argon in the gas mixture (E2 and E3), whereas they are seldom present in the case of Ar/H_2 mixture except at the end of E8. The same applies to Cr I lines, although they are more frequently seen than iron lines. This can be partly explained by the cooling of the plasma when hydrogen is added (Mauer, 2021), which can affect the evaporation of species into the plasma from the crucible.

In comparison, Mg I is frequently seen in the spectra with PL2 (E7 and E8). The arc frequently wanders towards the furnace walls, and thus the Mg I could also originate from the refractory lining. Calcium emission lines are present in all the experiments, indicating that there is a minor amount of residue slag or impurities within the furnace. The Mn I emission intensities, on the other hand, are much higher in Fig. 9 b) with a 50 mm electrode gap than a) with a 40 mm gap. Looking at Figs. 8 b) and Fig. 9 b), most of the emission lines' intensities rapidly increase near the end of E8. The instance before this increase corresponds to the spectrum and image of Fig. 4 h), and after the increase Fig. 4 i) and j). The difference lies in the status of the steel crucible, as the surface of it has clearly melted in Fig. 4 i) and j) in comparison to mostly solid state of h).

Towards the end of E8, the arc becomes more stable but does not reside at the center of the furnace. Fig. 10 shows that, at the end of E8, the arc hit the crucible wall and melted it. Also, the refractory was slightly melted near this location. The partial meltdown of the crucible and refractory lining, with an MgO content of 97%, can be seen in the time evolution of the emission lines in Fig. 9 b) where there is a sharp increase in the emission line intensities towards the end of E8. This kind of information on the meltdown of the crucible or refractory lining could prove to be vital in e.g. bigger furnaces where there is no clear view or safe place for a camera to see into the furnace.

In addition to atomic optical emissions from the Ca I and Ca II, also molecular optical emissions from CaO were detected in the spectra. Fig. 11 showcases such a spectrum from E7, together with the four most intensive H I lines, a few Ca I and Ar lines, two Na I lines, and a Li I line. Instead of sharp emission lines, the optical emissions from a molecule form broad emission bands. As demonstrated by Bol'shakov et al. (Bol'shakov et al., 2017) in a laser induced breakdown spectroscopy study, CaO has two bands near 560 and 625 nm. Similar band structure can be seen in the spectrum of Fig. 11. Clear detection of common slag components in Figs. 8 and 9 is a promising result when considering the prospects of on-line slag composition analysis for the HPSR process once the iron ore is reduced in the furnace.

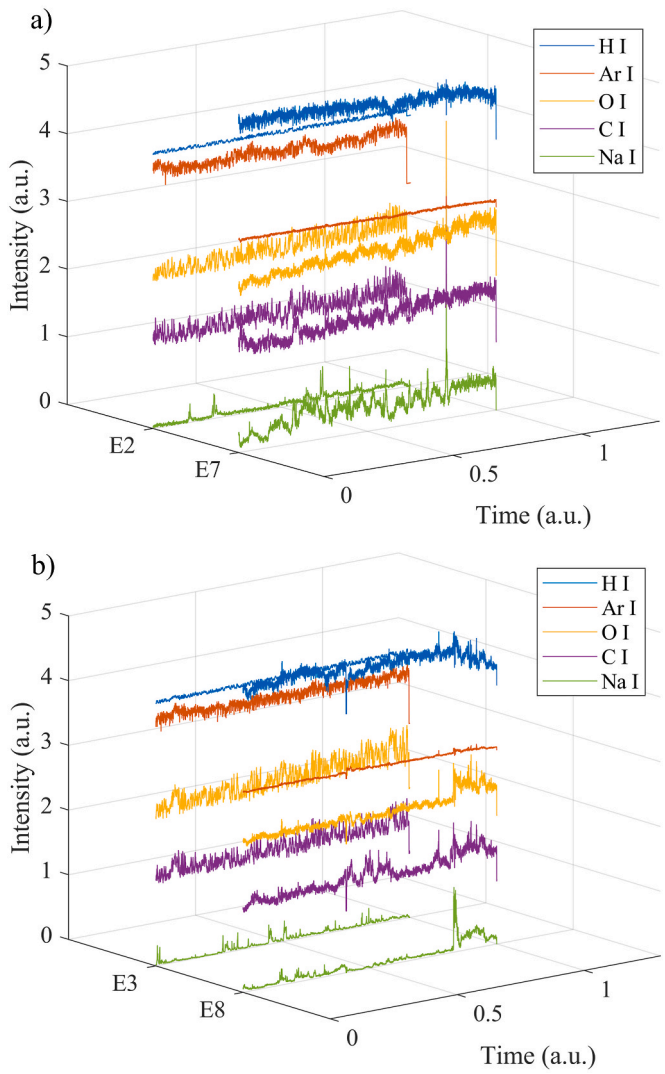

Fig. 8. Time evolution of H I, Ar I, O I, C I, and Na I from start to end of a) E2 and E7, b) E3 and E8. Each element has been normalized with respect to maximum intensity of a) E2 or E7 and b) E3 or E8. The time has been normalized for better comparison so that 0 and 1 correspond to the start and the end of experiment, respectively. An off-set has been applied to each emission line to improve the readability.

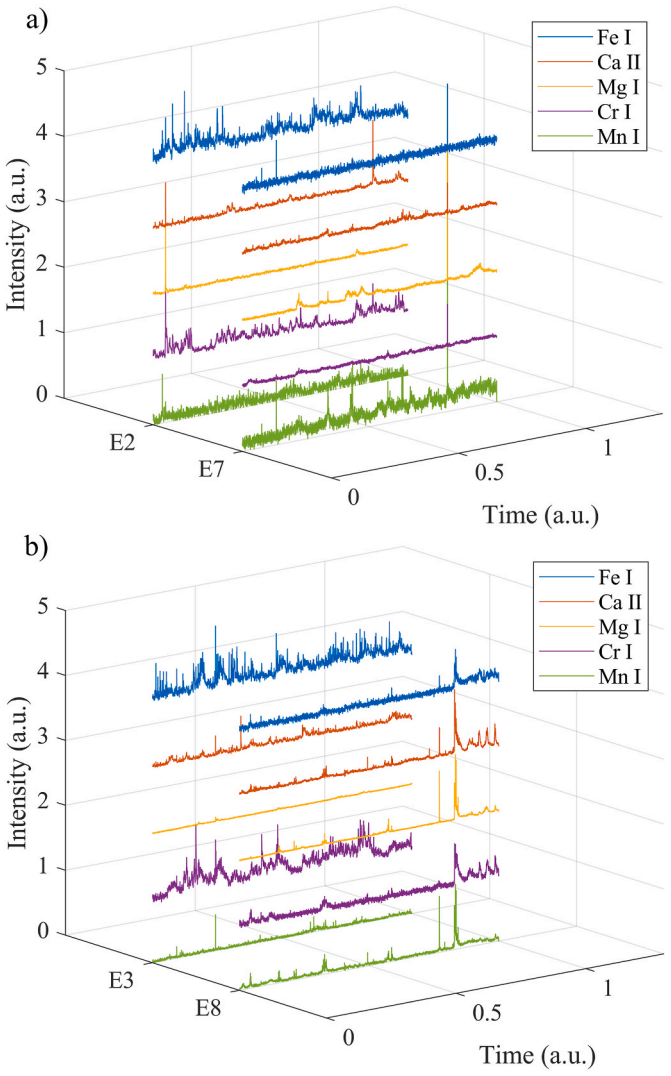

Fig. 9. Time evolution of Fe I, Ca II, Mg I, Cr I, and Mn I from start to end of a) E2 and E7, b) E3 and E8. Each slag species has been normalized with respect to maximum intensity of a) E2 or E7 and b) E3 or E8. The time has been normalized for better comparison so that 0 and 1 correspond to the start and the end of experiment, respectively. An off-set has been applied to each emission line to improve the readability.

Arc stability is an important factor in the HPSR so that the energy and hydrogen delivered to the iron ore are optimized. However, on a pilot or industrial scale, there usually is not a view into the furnace to see whether the arc resides near the center. One route to study the arc's position and properties would be to use OES in conjunction with the furnace data to provide information on the arc's position. In this study, it was observed that the voltage tends to increase with increasing arc length in E5-E8 with 40% H_2 in the gas flow. The electrode gap was kept constant in an experiment, and thus the increase in arc length is caused by the arc wandering away from the central position towards the furnace walls. In addition to this, the FWHM value of the H_β line was generally widest when the arc was near the central position, decreasing as the arc length increased. This behavior has been illustrated in Fig. 12 for E5-E7. The blue vertical lines show the sum of blue pixel brightness exceeding 250 at the camera's 0 to 255 scale at the center of the crucible. The blue pixels get to 250 and above only when the center of the arc is in the view, and thus it may be used as an indicator of whether the arc is at the central position. The dotted lines correspond either to the voltage values or the FWHM of the H_β line. As can be seen from the graphs, the voltage values are the lowest, and the FWHM values are the highest when the arc is in the center. This can clearly be seen especially in Fig. 12 c) in E7, which has a higher power level than a) and b).

The electrode gap and current were kept constant during each experiment, and the arc's movement on the surface of the crucible caused changes to the voltage and the power. The lower the voltage is, the shorter the arc length is and the closer the arc is to the central position. Changes in the FWHM values, on the other hand, are related to changes in the electron density. A longer arc encapsulates a larger volume than a short arc and since the FWHM increases by electrons colliding with the particles in the plasma, a longer arc length and consequently lower electron density bring down the FWHM.

The background that is seen in the spectra is not thermal radiation from the hot surface of the crucible, since the spectrum background disappears immediately when the arc is switched off, i.e. the spectrometer that looks into the furnace horizontally does not see the surface of the crucible. In addition, the background does not fit well with Planck's law, and thus it probably does not originate from heat radiation. The background radiation could originate from molecular optical emissions, which usually consist of many emission lines that may be very

Fig. 10. Image of the steel crucible and refractory after E8.

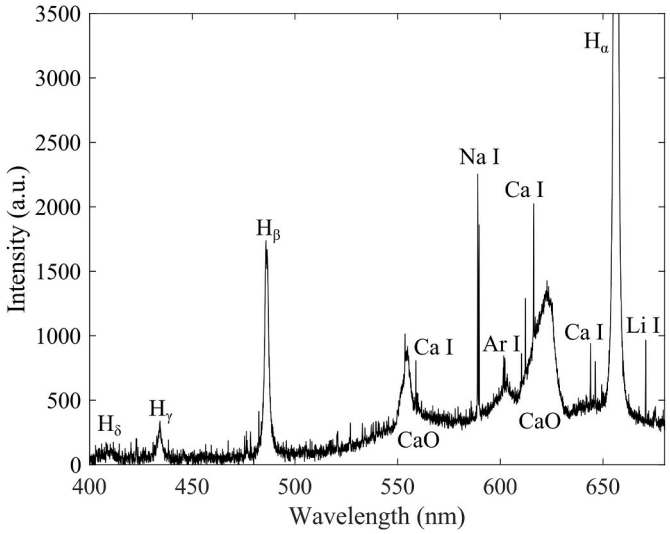

Fig. 11. An example spectrum from E7 showing the hydrogen lines, few Ar I, Na I, Li I, and Ca I lines, and CaO molecular optical emissions.

broad and overlap with one another, or from larger particles.

Fig. 13 shows how the background radiation behaves during the trials and how it relates to the central position of the arc. The intensity of the background radiation can be seen in Fig. 1 a), d), e), f), g), and i) as a broader intensity distribution on top of which the emission lines reside. In Fig. 13, a higher background is observed usually when the arc is close to or at the center of the crucible. However, there are few exceptions, as can be seen e.g. in Fig. 13 d) around 20 s, e) around 100 s, f) where the arc stays at the center only for short time, g) around 0 and 30 s, and h) during several occasions in E8.

Another measurement trial was conducted to study the origin of the background radiation. The H_2 content was gradually increased from near 0% to about 40% in the gas flow by keeping the total gas flow at 5 l/min. Fig. 14 illustrates this trial with information on the time evolution of the background radiation and Ar I 763 nm intensities, Ar and H plasma temperatures, electron density, the Ar and H_2 content in the off-gas, and background radiation as a function of Ar I 763 nm emission line intensity.

In Fig. 14, the arc stays out of view of the camera from 20 to 200 s and goes to the left-hand side of the view into the furnace between 200 and 260 s. The view into the furnace in this experiment was like the arc images in Fig. 4. From 0 to 260 s, the intensities of Ar I and background intensity have almost a linear relation with one another, as can be seen from Fig. 14 e). When the relative amount of Ar/H_2 in the gas flow changes and the arc is not at the center of the crucible, it seems that the background radiation and Ar I line intensities have similar time evolution. The background does not show this similar behavior with any other optical emission line in the spectra. However, between 260 and 325 s, the arc first jumps to the right-hand side of the furnace and then travels near to the center of the crucible. During this time, the Ar I intensity stays relatively stable even though Ar content in the gas flow decreases steadily, but the background radiation increases significantly. Thus, the Ar I excitation conditions stay relatively unchanged, but something changes in the background. One reason for this could be that the arc interacts more with gas flow from the hollow electrode when the arc goes near the arc center, thus increasing the radiation that is associated with the arc's interaction with the gas flow.

Based on Figs. 11 and 12, it seems that, at a constant Ar/H_2 ratio in the flow, an increase in the background radiation is usually a sign that the arc is near the center of the crucible. Additionally, the Ar I intensity starts to decline once H_2 is introduced to the gas flow and stays relatively constant above 23% H_2 content. This is in line with the discussion to Fig. 4 and the significant drop in Ar I emission line intensities when hydrogen is added to the gas.

Fig. 14 b) shows the plasma temperatures that have been derived with Equation (1) using Ar I and H I lines. In general, the Ar plasma temperature decreases as the Ar/H_2 decreases in the gas flow. During 200 and 333 s, when the arc starts to wander towards the center of the crucible, the Ar temperature fluctuates between 4500 and 10000 K and there are several occasions where self-absorption makes the plasma analysis unreliable. H I lines are also seen in the spectra without H_2 in the gas flow, which could arise from hydrogen in the atmosphere or residue water that has been absorbed by the refractory in an earlier experiment. H temperature shows relatively high temperatures before H_2 is introduced into the gas flow, i.e. during 0 and 60 s. This highly changing plasma temperature could well be caused by line fitting issues due to relatively low intensities of the H_β and H_γ lines, which were used for the temperature analysis together with H_α line. However, even with the small amount of H_2 that is added to the gas around 60 s, the H plasma temperature stabilizes and drastically decreases with a mean value of 3610 K between 60 and 200 s. Between 200 and 333 s, the mean H temperature is 3460 K.

The electron density, and consequently the FWHM of H_α line, do not show a clear trend with changing Ar and H_2 content in the gas flow. However, the increase of the electron density between 160 and 190 s is not actually caused by an increase in the FWHM but by a distorted line profile of the H_α, where the intensity of the H_α is saturated. At around 200 s when the arc starts to wander towards the center of the crucible, the electron density first drops around 200 s and then gradually increases towards the end. This, in turn, is in line with the statement that electron density increases as the arc length decreases. Due to the changing the position of the arc during the experiment for Fig. 14, a clear dependence between e.g. gas flow composition and electron density cannot be deduced. Thus, it should be emphasized that the changes in the arc's position on the crucible should be considered when comparing the values of Fig. 14 to one another.

5. Conclusions

In this study, hydrogen plasma used for HPSR has been studied with

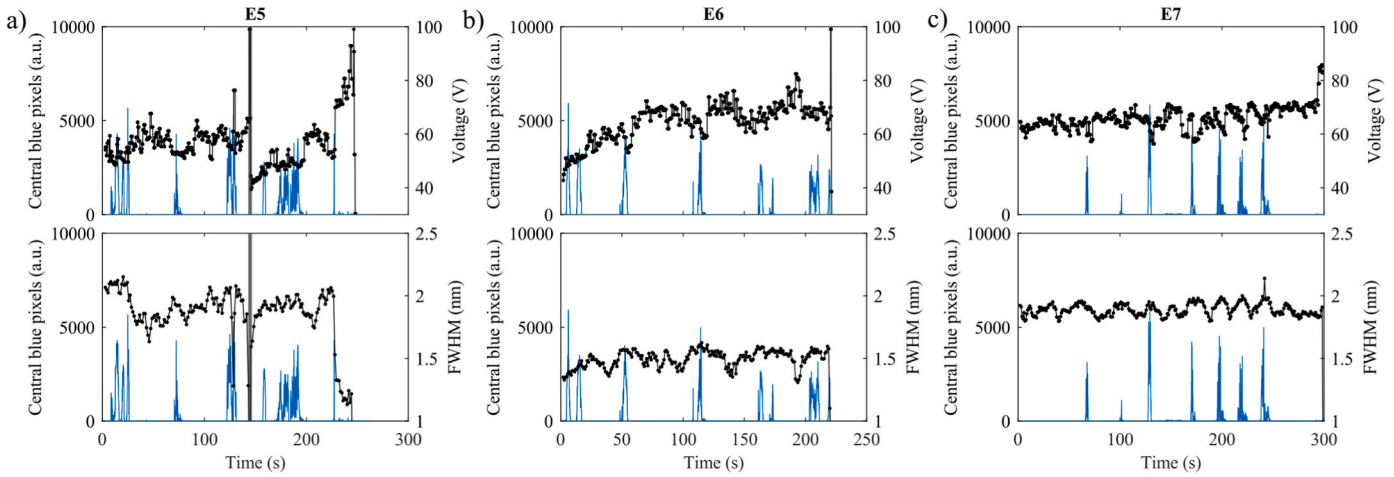

Fig. 12. Sum of blue pixels at the center of the crucible together with the voltage and FWHM of H_β line for a) E5, b) E6, and c) E7. The arc extinguished during E5 at the instance with the solid vertical line at 145 s.

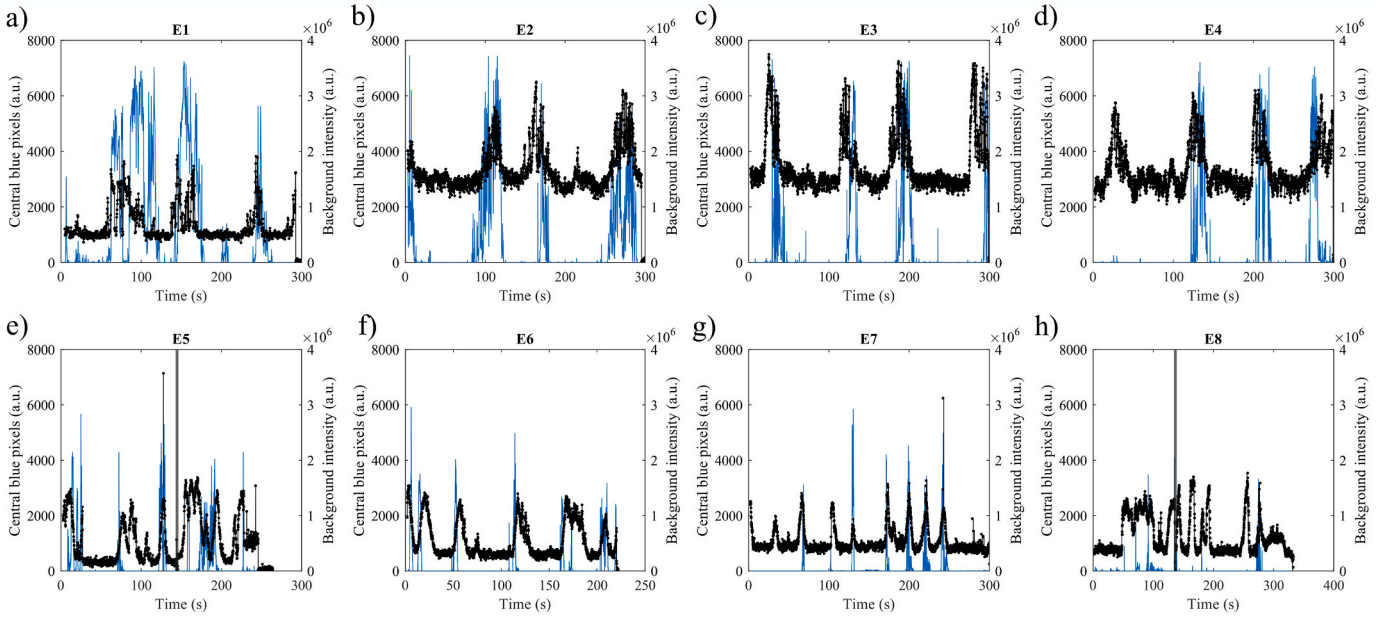

Fig. 13. Sum of blue pixels at the center of the crucible together with the background radiation intensity for a) E1, b) E2, and c) E3, d) E4, e) E5, f) E6, g) E7, and h) E8. The arc extinguished during E5 and E8 at the instance with the solid vertical line.

optical emission spectroscopy, arc image analysis, and plasma diagnostics. The results show that OES can be used to obtain spectra from the HPSR plasma, paving the way for a more detailed OES analysis during iron ore reduction studies. The set of experiments shed light on how the arc behaves with respect to changing electrode gap and gas composition up to 40% H_2. The time evolution of Ar I and H I together with optical emission lines from iron and common slag components varied significantly in different experiments. Together with the arc image analysis, OES data, and electrical data of the furnace, the position of the arc on the crucible could be determined by looking at the voltage, FWHM values of H_α line, and background radiation intensity. Near-center positioning of the arc is essential for optimized reduction, especially if the iron ore is fed into the furnace through a hollow electrode. Identification of common slag components from the spectra of this study also shows prospects for slag composition assessment during the HPSR process with the OES. Additionally, OES can be used to detect, e.g., if the crucible starts to melt, as described in the discussion related to experiment 8.

The experiments also showed that the gap between the electrode and the crucible together with the power level has to be selected so that the process is optimized. In the present work, the arc hit the crucible wall and melted it with a 50 mm gap and power level 2 toward the end of experiment 8. In this regard, a lower electrode gap could be used, as was done in experiment 7 with a 40 mm gap and power level 2. Usage of a higher power level might be necessary for an optimized reduction process, and thus adjusting the electrode gap accordingly could prove to be necessary to reduce the movement of the arc. In Ar/H_2 plasma, the estimated electron density dropped 26% when the electrode gap was increased from 3 to 4 cm with PL1, and 17% when the gap was increased from 4 to 5 cm with PL2. The ionization degree of the plasma has a key role in the reduction kinetics, and thus these parameters should be considered also from reaction kinetics point of view to optimize the HPSR process.

When considering the HPSR as a whole, OES data can provide information on the composition of the plasma, the condition of the reduction, as well as the position of the plasma for optimized reduction

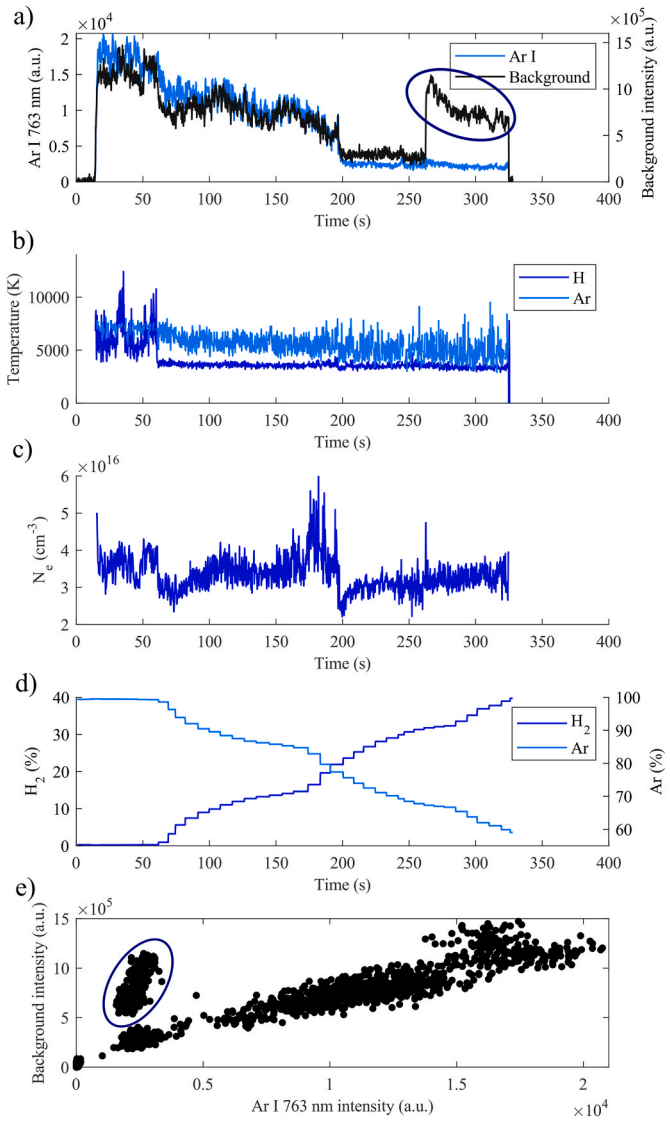

Fig. 14. An experiment with gradually increasing H_2 content showing a) the time evolution of the Ar I 763 nm emission line and background radiation, b) plasma temperatures derived with Ar and H lines, c) estimate on the electron density derived with FWHM of H_α, d) time evolution of Ar and H_2 content in the off-gas, and e) background radiation as a function of Ar I 763 nm emission line intensity. The circles in a) and e) reflect the period when the arc is near the center of the crucible towards the end of the trial.

for iron ore that is fed into the furnace e.g. through an HGE. For the purposes of on-line process control, an OES data analysis algorithm deriving all the aforementioned parameters from the spectra would be beneficial in future studies to see how OES can be used to optimize the reducing conditions during iron ore reduction. Due to the easy-to-use equipment of OES and HPSR as an intensive source of light from the plasma, OES shows great promise in developing a better understanding of the HPSR and how the process can be optimized further. The limitations of OES for HPSR process monitoring are mostly related to the visibility of the arc and whether or not a clear view into the furnace can be provided for the optical fiber. In this study, the spectra could be recorded even though the arc moved occasionally, but introducing e.g. fine iron ore for the reduction will most probably result in dust as well as water vapor in the atmosphere. Assessing how these species in the furnace atmosphere will absorb light and how their effect on the spectra can be mitigated will be a major topic for future studies.

With the experimental procedures and methods that were established in this article, the next steps would be to use OES in conjunction with arc images to study the reduction of iron ore. Future work should include using OES to characterize and analyze the status of the HPSR with special emphasis on assessing how the reaction kinetics could be studied. Another interesting topic will be to study different flow rates for the input gas to analyze how the gas flow affects the intensity of the background radiation.

CRediT authorship contribution statement

Henri Pauna: Methodology, Formal analysis, Writing – original draft, Writing – review & editing, Visualization. **Daniel Ernst:** Conceptualization, Methodology, Investigation, Resources, Writing – original draft, Writing – review & editing, Visualization. **Michael Zarl:** Conceptualization, Methodology, Investigation, Resources. **Matti Aula:** Writing – review & editing, Supervision. **Johannes Schenk:** Writing – review & editing, Supervision. **Marko Huttula:** Writing – review & editing, Supervision. **Timo Fabritius:** Writing – review & editing, Supervision.

Declaration of competing interest

The authors declare that they have no known competing financial interests or personal relationships that could have appeared to influence the work reported in this paper.

Data availability

The data that has been used is confidential.

Acknowledgments

Funding: This work was supported by the Academy of Finland under the Genome of Steel grant No. 311934, Business Finland with the Towards Fossil-free Steel project No. 45774/31/2020, and the COMET program Fundamentals of hydrogen reduction, K1-MET project number 12204396. COMET is funded by the Federal Ministry for Climate Action, Environment, Energy, Mobility, Innovation, and Technology, the Federal Ministry for Digital and Economic Affairs, the provinces of Upper Austria, Tyrol, and Styria, and the Styrian Business Promotion Agency (SFG). In addition, this work is partially financed by the industrial partners voestalpine Stahl GmbH and voestalpine Stahl Donawitz GmbH and the scientific partner Montanuniversitaet Leoben.

References

Aragón, C., Aguilera, J.A., 2008. Characterization of laser induced plasmas by optical emission spectroscopy: a review of experiments and methods. Spectrochim. Acta B 63, 893–916. https://doi.org/10.1016/j.sab.2008.05.010.

Bol'shakov, A.A., Mao, X., Russo, R.E., 2017. Spectral emission enhancement by an electric pulse for LIBS and LAMIS. J. Anal. At Spectrom 32, 657. https://doi.org/10.1039/C6JA00436A.

Chauvy, R., Weireld, G. de, 2020. CO 2 utilization technologies in europe: a short review. Energy Technol. 8, 2000627 https://doi.org/10.1002/ente.202000627.

Draxler, M., Schenk, J., Bürgler, T., Sormann, A., 2020. The steel industry in the European union on the crossroad to carbon lean production—status, initiatives and challenges. Berg Huettenmaenn Monatsh. 165, 221–226. https://doi.org/10.1007/s00501-020-00975-2.

Ernst, D., Zarl, M.A., Cejka, J., Schenk, J., 2022. A new methodological approach on the characterization of optimal charging rates at the hydrogen plasma smelting reduction process Part 2: results. Materials 15, 4065. https://doi.org/10.3390/ma15124065.

Eurofer The European Steel Association. Low carbon roadmap: pathways to a CO2-neutral European steel industry [Online], 2019. Available online: https://www.eurofer.eu/assets/Uploads/EUROFER-Low-Carbon-Roadmap-Pathways-to-a-CO2-neutral-European-Steel-Industry.pdf.

Hainsch, K., Löffler, K., Burandt, T., Auer, H., Crespo del Granado, P., Pisciella, P., Zwickl-Bernhard, S., 2022. Energy transition scenarios: what policies, societal attitudes, and technology developments will realize the EU Green Deal? Energy 239, 122067. https://doi.org/10.1016/j.energy.2021.122067.

Holappa, L., 2020. A general vision for reduction of energy consumption and CO2 emissions from the steel industry. Metals 10, 1117. https://doi.org/10.3390/met10091117.

Masab Naseri Seftejani, 2020. Reduktion von Hämatit mittels Wasserstoffplasma-Schmelzreduktion. Dissertation. Montanuniversität Leoben.

Mauer, G., 2021. How hydrogen admixture changes plasma jet characteristics in spray processes at low pressure. Plasma Chem. Plasma Process. 41, 109–132. https://doi.org/10.1007/s11090-020-10143-6.

Naseri Seftejani, M., Schenk, J., 2018a. Thermodynamic of liquid iron ore reduction by hydrogen thermal plasma. Metals 8, 1051. https://doi.org/10.3390/met8121051.

Naseri Seftejani, M., Schenk, J., 2018b. Fundamentals of Hydrogen Plasma Smelting Reduction (HPSR) of Iron Oxides, a New Generation of Steelmaking Processes.

Quader, M.A., Ahmed, S., Ghazilla, R.A.R., Ahmed, S., Dahari, M., 2015. A comprehensive review on energy efficient CO2 breakthrough technologies for sustainable green iron and steel manufacturing. Renew. Sustain. Energy Rev. 50, 594–614. https://doi.org/10.1016/j.rser.2015.05.026.

Rieger, J., Colla, V., Matino, I., Branca, T.A., Stubbe, G., Panizza, A., Brondi, C., Falsafi, M., Hage, J., Wang, X., et al., 2021. Residue valorization in the iron and steel industries: sustainable solutions for a cleaner and more competitive future europe. Metals 11, 1202. https://doi.org/10.3390/met11081202.

Sabat, K.C., Murphy, A.B., 2017. Hydrogen plasma processing of iron ore. Metall. Mater. Trans. B 48, 1561–1594. https://doi.org/10.1007/s11663-017-0957-1.

Souza Filho, I.R., Springer, H., Ma, Y., Mahajan, A., da Silva, C.C., Kulse, M., Raabe, D., 2022. Green steel at its crossroads: hybrid hydrogen-based reduction of iron ores. J. Clean. Prod. 340, 130805 https://doi.org/10.1016/j.jclepro.2022.130805.

Sun, L., Yu, A., 2009. Correction of self-absorption effect in calibration-free laser-induced breakdown spectroscopy by an internal reference method. Talanta 79, 388–395. https://doi.org/10.1016/j.talanta.2009.03.066.

Suopajärvi, H., Umeki, K., Mousa, E., Hedayati, A., Romar, H., Kemppainen, A., Wang, C., Phounglamcheik, A., Tuomikoski, S., Norberg, N., et al., 2018. Use of biomass in integrated steelmaking – status quo, future needs and comparison to other low-CO2 steel production technologies. Appl. Energy 213, 384–407. https://doi.org/10.1016/j.apenergy.2018.01.060.

Surmick, D., Parigger, C., 2014. Empirical formulae for electron density diagnostics from Hα and Hβ line profiles. Int. Rev. At. Mol. Phys. 5, 73.

World Steel Association AISBL, 2021. World Steel in Figures [Online]. Available online: https://worldsteel.org/wp-content/uploads/2021-World-Steel-in-Figures.pdf. (Accessed 15 February 2022).

Zarl, M.A., Farkas, M.A., Schenk, J., 2020. A study on the stability fields of arc plasma in the HPSR process. Metals 10, 1394. https://doi.org/10.3390/met10101394.

Zarl, M.A., Ernst, D., Cejka, J., Schenk, J., 2022. A new methodological approach to the characterization of optimal charging rates at the hydrogen plasma smelting reduction process Part 1: method. Materials 15, 4767. https://doi.org/10.3390/ma15144767.

Zhao, J., Zuo, H., Wang, Y., Wang, J., Xue, Q., 2020. Review of green and low-carbon ironmaking technology. Ironmak. Steelmak. 47, 296–306. https://doi.org/10.1080/03019233.2019.1639029.